Astronomy & Astrophysics

LETTER TO THE EDITOR

Discovery of CH_2CCHC_4H and a rigorous detection of CH_2CCHC_3N in TMC-1 with the QUIJOTE line survey[⋆],[⋆⋆]

R. Fuentetaja[1], C. Cabezas[1], M. Agúndez[1], B. Tercero[2,3], N. Marcelino[3], J. R. Pardo[1],
P. de Vicente[2], and J. Cernicharo[1]

[1] Dpt. de Astrofísica Molecular, Instituto de Física Fundamental (IFF-CSIC), C/ Serrano 121, 28006 Madrid, Spain
e-mail: r.fuentetaja@csic.es, jose.cernicharo@csic.es
[2] Centro de Desarrollos Tecnológicos, Observatorio de Yebes (IGN), 19141 Yebes, Guadalajara, Spain
[3] Observatorio Astronómico Nacional (OAN, IGN), Madrid, Spain

ABSTRACT

Using the QUIJOTE line survey in the 32.0–50.4 GHz range, we report the discovery of the molecule CH_2CCHC_4H towards the prestellar cold core TMC-1 in the Taurus region. We also present a rigorous detection of CH_2CCHC_3N, along with its detailed analysis. We identified a total of twenty rotational transitions for each one of these molecules. The rotational quantum numbers range from $J_u = 17$ up to 24 and $K_a \leq 3$. The column density for CH_2CCHC_4H is $N = (2.2 \pm 0.2) \times 10^{12}$ cm^{-2}, while for CH_2CCHC_3N, we derived $N = (1.2 \pm 0.15) \times 10^{11}$ cm^{-2}. The rotational temperature is 9.0 ± 0.5 K for both species. The abundance ratio between CH_2CCHC_4H and CH_2CCHC_3N is 18 ± 4. We also compared the column densities of these species with those of their isomers CH_3C_6H and CH_3C_5N, derived from their $J = 20 - 10$ up to $J = 31 - 30$ rotational transitions observed with the QUIJOTE line survey. The observed abundances for all these species are reasonably well explained by state-of-the-art chemical models of TMC-1. The observed astronomical frequencies were merged with laboratory frequencies from the literature to derive improved spectroscopic parameters.

Key words. molecular data – line: identification – ISM: molecules – ISM: individual objects: TMC-1 – astrochemistry

1. Introduction

The recent results obtained towards TMC-1 with the Yebes 40 m radio telescope through the QUIJOTE (*Q*-band Ultrasensitive Inspection Journey to the Obscure TMC-1 Environment) line survey (Cernicharo et al. 2021a) and those of the Green Bank 100 m telescope with the GOTHAM survey (McGuire et al. 2018) show that this source presents a paramount challenge to our understanding of the chemical processes in cold prestellar cores. Several cyclic molecules have been detected such as cyclopentadiene and indene (Cernicharo et al. 2021b), as well as ortho-benzyne (Cernicharo et al. 2021a), the cyano derivatives of cyclopentadiene, benzene, and naphthalene (McGuire et al. 2018, 2021; McCarthy et al. 2021; Lee et al. 2021), and the ethynyl derivatives of cyclopentadiene (Cernicharo et al. 2021c). Moreover, several extremely abundant hydrocarbons such as propargyl (Agúndez et al. 2021), vinyl acetylene (Cernicharo et al. 2021d), and allenyl acetylene (Cernicharo et al. 2021e) have also been discovered towards TMC-1. Most of these species had not been predicted to exhibit a significant abundance in chemical models prior to their detec-

tions. These results indicate that key chemical processes involving hydrocarbons (radical, neutral, ion-neutral, and perhaps dust grain surface reactions) have been neglected in previous chemical networks. Thus, a new chemistry is emerging based on these TMC-1 observations.

The study of ethynyl and cyanide derivatives of hydrocarbons is of paramount importance, as they can allow us to follow the different chemical paths to produce them from a common precursor through reactions involving the CCH and CN radicals (Cernicharo et al. 2021f). In this regard, the discovery in TMC-1 of various isomers with formulae C_5H_4 and C_4H_3N allows us to also constrain the chemical schemes behind their formation (Cernicharo et al. 2021e; Marcelino et al. 2021). These schemes involve reactions of CCH and CN with the hydrocarbons CH_3CCH and CH_2CCH_2, allowing for an indirect estimation of the abundance of the non-polar but abundant hydrocarbon allene to be made. The same chemical schemes leading to C_5H_4 and C_4H_3N isomers can be extended to longer species by substituting the radicals CCH and CN by their longer equivalents C_4H and C_3N, which would result in different isomers with formula C_7H_4 and C_6H_3N.

In this Letter, we report the discovery of CH_2CCHC_4H (allenyl diacetylene) using a line survey performed with the Yebes 40 m telescope (QUIJOTE; see Cernicharo et al. 2021a). This species is an isomer of CH_3C_6H, both with the formula C_7H_4. We also present a detailed study and a rigorous and robust detection of CH_2CCHC_3N, an isomer of CH_3C_5N (both with formula C_6H_3N) which was recently claimed through stacking

techniques by Shingledecker et al. (2021). Each of these large species has small rotational constants. These, together with an unbiased line surveys such as QUIJOTE, allow studying many rotational transitions and, hence, to derive homogeneous and realistic values of their column densities. We investigate the chemistry of these species with the aid of updated gas-phase chemical models.

2. Observations

New receivers built within the Nanocosmos project[1] and installed at the Yebes 40 m radiotelescope were used for the observations of TMC-1 (α_{J2000} = $4^h41^m41.9^s$ and δ_{J2000} = +25°41′27′′.0). A detailed description of the system is given by Tercero et al. (2021). The receiver consists of two cold high electron mobility transistor amplifiers covering the 31.0–50.3 GHz band with horizontal and vertical polarizations. Receiver temperatures in the runs achieved during 2020 vary from 22 K at 32 GHz to 42 K at 50 GHz. Some power adaptation in the down-conversion chains effectively reduced the receiver temperatures during 2021 to 16 K at 32 GHz and 30 K at 50 GHz. The backends are $2 \times 8 \times 2.5$ GHz fast Fourier transform spectrometers with a spectral resolution of 38.15 kHz, providing full coverage of the Q-band in both polarizations.

A detailed description of the QUIJOTE line survey is provided in Cernicharo et al. (2021a). In brief, the present data come from several observing runs between December 2019 and January 2022. All observations were performed in the frequency-switching mode with frequency throws of 8 and 10 MHz. The total on-source observing time for data taken with frequency throws of 8 MHz and 10 MHz is 173.1 and 253.6 h, respectively. Hence, the total observing time on source by December 2021 is 426.7 h. The measured sensitivity varies between 0.12 mK at 32 GHz and 0.25 mK at 49.5 GHz. For each frequency throw, different local oscillator frequencies were used in order to remove possible side band effects in the down conversion chain.

The main beam efficiency varies from 0.6 at 32 GHz to 0.43 at 50 GHz (Tercero et al. 2021). Pointing corrections were derived from nearby quasars and SiO masers and the errors were always within 2–3′′. The telescope beam size is 56′′ and 31′′ at 31 and 50 GHz, respectively. The intensity scale used in this work, antenna temperature (T_A^*), was calibrated using two absorbers at different temperatures and the atmospheric transmission model ATM (Cernicharo 1985; Pardo et al. 2001). The adopted calibration uncertainties are at the level of 10% and all the data were analysed using the GILDAS package[2].

3. Results

The line identification in this work has been achieved using the MADEX (Cernicharo 2012), CDMS (Müller et al. 2005), and JPL (Pickett et al. 1998) catalogues. By April 2021, the MADEX has featured 6433 spectral entries corresponding to the ground and vibrationally excited states, together with the corresponding isotopologues of 1733 molecules.

3.1. Discovery of CH_2CCHC_4H

The search for new species in our survey is based on intensity predictions for the molecules for which their rotational spectroscopy

is available. The sensitivity of QUIJOTE is a factor ~50 larger than that of previous TMC-1 Q-band line surveys (Kaifu et al. 2004), which has permitted us to address the search of molecules with a very low dipole moment (Cernicharo et al. 2021a). Taking into account the large abundances derived from QUIJOTE's data for hydrocarbons such as CH_2CHCCH (Cernicharo et al. 2021d), CH_2CCH (Agúndez et al. 2021, 2022), $CH_2CCHCCH$ (Cernicharo et al. 2021e), H_2C_5 (Cabezas et al. 2021), c-C_6H_4 (Cernicharo et al. 2021a), c-C_5H_6, and c-C_9H_8 (Cernicharo et al. 2021d), other similar species could be present in the survey, such as allenyl diacetylene (CH_2CCHC_4H). Rotational spectroscopy for this species has been measured in the laboratory by McCarthy et al. (2020). We fitted these lines and implemented the rotational constants into MADEX (Cernicharo 2012). The derived constants, given in Table B.1, are identical to those of McCarthy et al. (2020). We predicted the intensities for all lines above 0.5 mK, adopting an initial column density of 5×10^{12} cm^{-2} and a rotational temperature of 10 K. Twenty lines of this species with intensities between 0.4 and 0.7 mK have been found with a signal-to-noise ratio (S/N) between 3 and 6. These are shown on Fig. 1 and the derived line parameters are given in Table A.1. Several lines are partially blended with other features, most of them arising from unknown species. Nevertheless, many lines appear as single features and provide a solid detection of this molecule.

Using the observed frequencies and those measured in the laboratory, we derived a new set of rotational and distortion constants. They are provided in Appendix B and Table B.1. The difference between observed and calculated values are given in Table B.3. The new constants are practically identical to those of McCarthy et al. (2020), but have lower uncertainties, which allow for more precise frequency predictions at higher frequencies.

To derive the column density and rotational temperature we used a model line fitting procedure (see e.g. Cernicharo et al. 2021d), which leads to N(CH_2CCHC_4H) = $(2.2 \pm 0.2) \times 10^{12}$ cm^{-2} and $T_{rot} = 9.0 \pm 0.5$ K. A rotational temperature lower than 8.5 K results on an underestimation of the observed intensity for transitions with $K_a = 2$. We assumed a source of uniform brightness with a diameter of 80′′ (Fossé et al. 2001; Cernicharo et al., in prep.). The predicted synthetic lines for these parameters are shown on Fig. 1 (red lines). Adopting a H_2 column density for TMC-1 of 10^{22} cm^{-2} (Cernicharo & Guélin 1987), the abundance of CH_2CCHC_4H is $(2.2 \pm 0.2) \times 10^{-10}$. Using a $CH_2CCHCCH$ column density of N = 1.2×10^{13} cm^{-2} (Cernicharo et al. 2021e), we derive a $CH_2CCHCCH/CH_2CCHC_4H$ abundance ratio of ~5.5, similar to the CCH/C_4H radicals abundance ratio of ~4 derived by Cernicharo et al. (in prep.).

3.2. A robust detection of CH_2CCHC_3N

CH_2CCHC_3N (cyanoacetyleneallene or 4.5-hexadien-2-ynenitrile) was recently reported as having been detected towards TMC-1 by Shingledecker et al. (2021). No individual lines were reported but the stacking of all lines within their line survey. In order to search for the lines of this species with QUIJOTE, we fit the rotational lines of this species kindly provided to us by M. McCarthy. Using these constants, we predicted the frequencies for all the lines of this molecule with $K_a \leq 3$ within the Q-band. Twenty eight lines were detected and their line parameters are given in Table A.1. Twenty of these lines are shown on Fig. 2. Although some lines are blended, the detection is now rigorous, as many individual lines are clearly seen in our data. Improved rotational and distortion constants are provided in Appendix B and Table B.2.
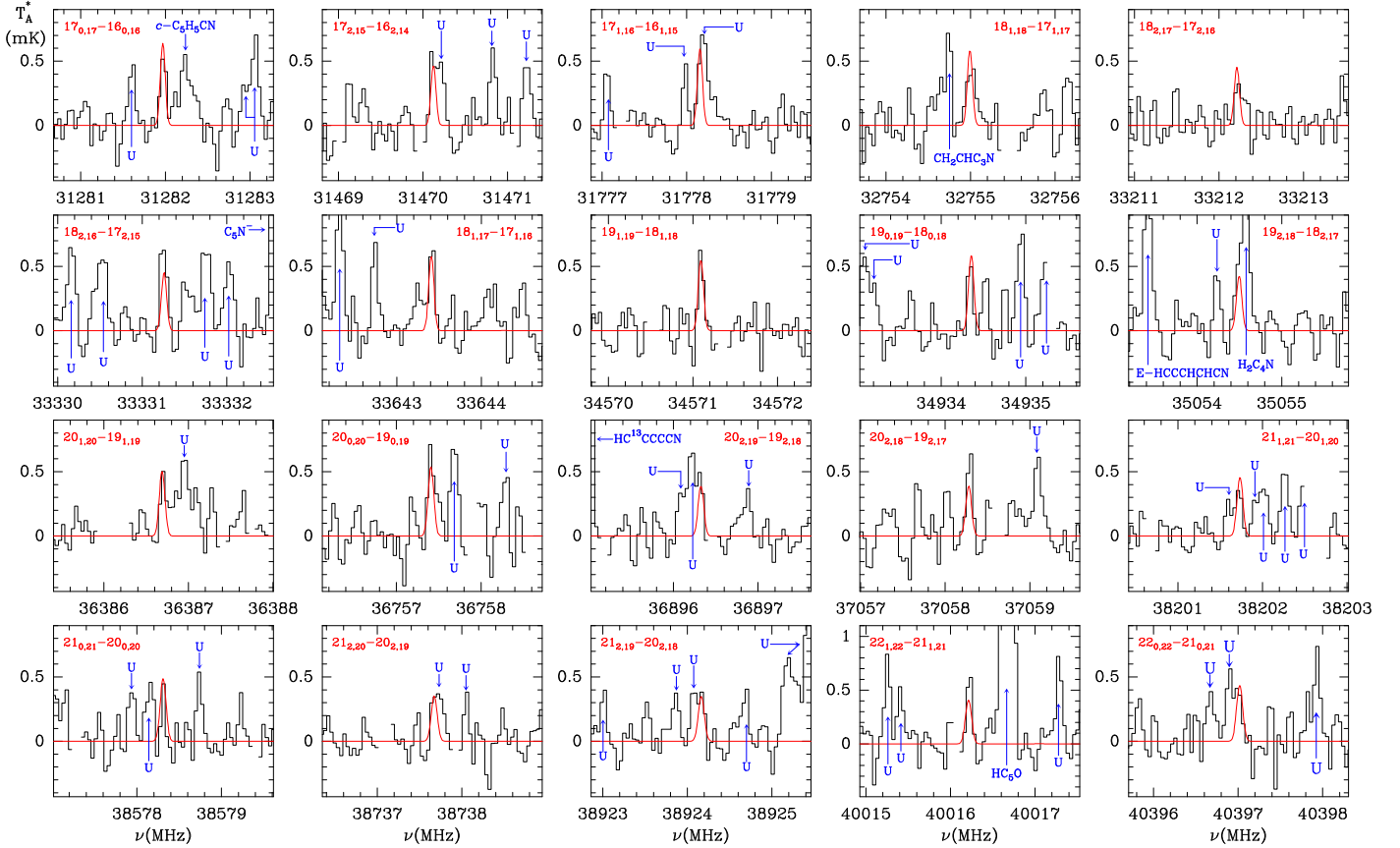
Fig. 1. Observed transitions of CH$_2$CCHC$_4$H in TMC-1. The abscissa corresponds to the rest frequency of the lines. Frequencies and intensities for the observed lines are given in Table A.1. The ordinate is the antenna temperature, corrected for atmospheric and telescope losses, in milliKelvin. The quantum numbers of each transition are indicated in the corresponding panel. Red line shows the computed synthetic spectrum for this species for $T_{\rm rot}$ = 9 K and a column density of 2.2×10^{12} cm^{-2}. Blanked channels correspond to negative features produced when folding the frequency-switched data.

We assumed the same source parameters than for CH$_2$CCHC$_4$H. Through a model fitting procedure, we derive a rotational temperature of 9.0 ± 0.5 K and a column density of $(1.20 \pm 0.15) \times 10^{11}$ cm^{-2}. Hence, the abundance of CH$_2$CCHC$_3$N is $(1.20 \pm 0.15) \times 10^{-11}$. Our column density agrees with the total value derived from the four velocity and source components of model B of Shingledecker et al. (2021) $(1.6 \times 10^{11}$ cm^{-2}, see their Table A.1). The results concerning their models A or C can be fully discarded, as they provide unreasonable rotational temperatures (model A) or extremely large column densities (model C). We consider that our determination based on the observation of many individual lines is more accurate. Hence, the CH$_2$CCHC$_4$H/CH$_2$CCHC$_3$N abundance ratio is 18 ± 4.

It is interesting to compare the column densities of the different ethynyl and cyanide derivatives of species containing the allenyl group CH$_2$CCH. To this purpose, we derived the column density of C$_4$H and C$_3$N from our data, and we found N(C$_4$H) = 1.1×10^{14} cm^{-2} and N(C$_3$N) = 1.4×10^{13} cm^{-2} (Cernicharo et al., in prep.). These values result in an abundance ratio C$_4$H/C$_3$N of 8, which is somewhat lower than the CH$_2$CCHC$_4$H/CH$_2$CCHC$_3$N ratio of 18 ± 4 derived in this work.
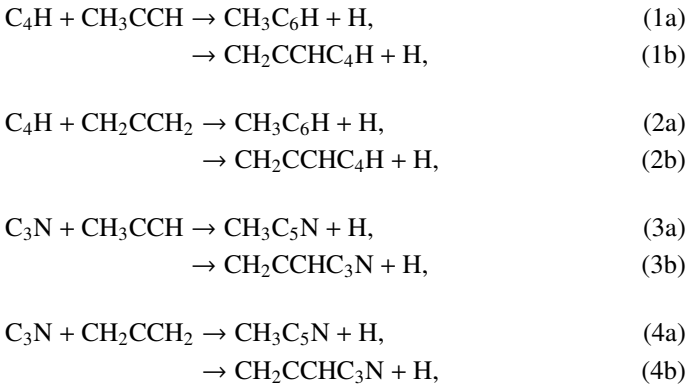
4. Discussion

For a better understanding of the formation of CH$_2$CCHC$_4$H and CH$_2$CCHC$_3$N, we carried out chemical model calculations. The

chemical model is similar to those presented in Marcelino et al. (2021) and Cernicharo et al. (2021e). Briefly, we adopted typical parameters of cold dark clouds, namely, a gas kinetic temperature of 10 K, a volume density of H nuclei of 2×10^4 cm^{-3}, a visual extinction of 30 mag, a cosmic-ray ionization rate of 1.3×10^{-17} s^{-1}, and the set of "low-metal" elemental abundances (Agúndez & Wakelam 2013). We adopted the chemical network RATE12 from the UMIST database (McElroy et al. 2013), updated to include the chemistry of C$_5$H$_4$, C$_7$H$_4$, C$_4$H$_3$N, and C$_6$H$_3$N. The chemistry of C$_5$H$_4$ and C$_4$H$_3$N isomers has been discussed by Cernicharo et al. (2021e) and Marcelino et al. (2021), respectively. In the case of C$_7$H$_4$ isomers, the main formation routes involve the dissociative recombination of C$_7$H$_5^+$ with electrons and the neutral-neutral reactions of the C$_4$H radical with CH$_3$CCH, CH$_2$CCH$_2$, and CH$_3$CHCH$_2$, while C$_6$H$_3$N is formed by the dissociative recombination of C$_6$H$_4$N$^+$ and the neutral-neutral reactions of the radical C$_3$N with CH$_3$CCH and CH$_2$CCH$_2$. The reactions involving C$_4$H have been experimentally studied by Berteloite et al. (2010), while those involving C$_3$N have been studied also experimentally by Fournier (2014). These reactions are found to be rapid at low temperatures, although information on the branching ratios of the different exothermic channels is not available. Therefore, in the chemical model, we do not distinguish between different isomers of C$_7$H$_4$ or C$_6$H$_3$N. The chemistry of these two isomeric families share similarities because an important part of the synthesis relies on the reaction of either C$_4$H or C$_3$N with methyl acetylene and allene. We may summarize these routes as:
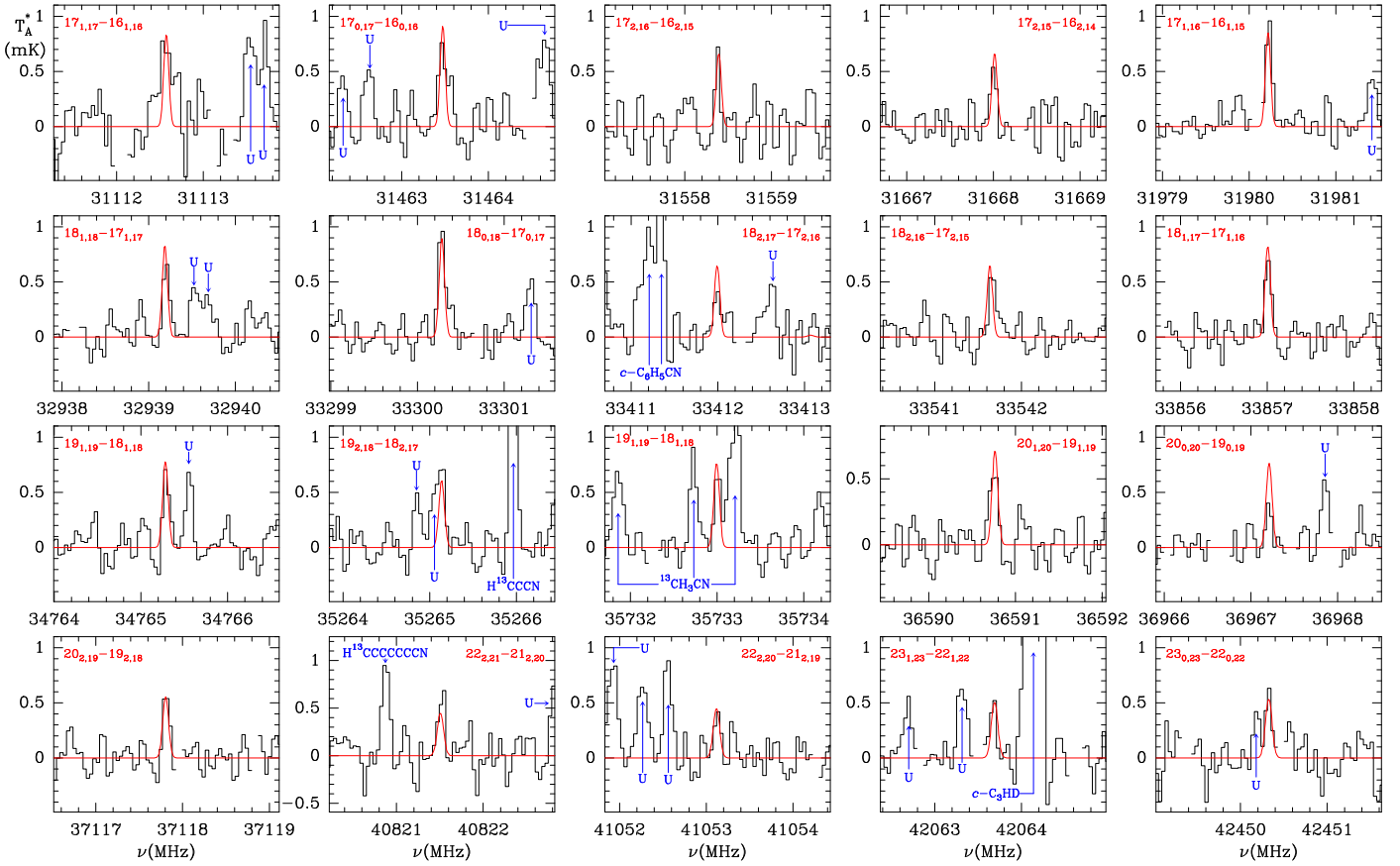
Fig. 2. Selected transitions of CH_2CCHC_3N in TMC-1. The abscissa corresponds to the rest frequency of the lines. Frequencies and intensities for all observed lines are given in Table A.1. The ordinate is the antenna temperature, corrected for atmospheric and telescope losses, in milliKelvin. The quantum numbers of each transition are indicated in the corresponding panel. The red line shows the computed synthetic spectrum for this species for $T_{rot} = 9$ K and a column density of 1.2×10^{11} cm^{-2}. Blanked channels correspond to negative features produced when folding the frequency-switched data.

$$C_4H + CH_3CCH \rightarrow CH_3C_6H + H, \qquad (1a)$$
$$\rightarrow CH_2CCHC_4H + H, \qquad (1b)$$

$$C_4H + CH_2CCH_2 \rightarrow CH_3C_6H + H, \qquad (2a)$$
$$\rightarrow CH_2CCHC_4H + H, \qquad (2b)$$

$$C_3N + CH_3CCH \rightarrow CH_3C_5N + H, \qquad (3a)$$
$$\rightarrow CH_2CCHC_3N + H, \qquad (3b)$$

$$C_3N + CH_2CCH_2 \rightarrow CH_3C_5N + H, \qquad (4a)$$
$$\rightarrow CH_2CCHC_3N + H, \qquad (4b)$$

where we only consider the C_7H_4 isomers CH_3C_6H and CH_2CCHC_4H because they are the only ones detected in TMC-1 although other C_7H_4 isomers could also be formed (see Berteloite et al. 2010). Similarly, only the C_6H_3N isomers CH_3C_5N and CH_2CCHC_3N are considered, but others can also be formed. We adopt as main destruction routes for C_7H_4 and C_6H_3N the reactions with the ions C^+, He^+, HCO^+, and H_3^+. In Fig. 3 we compare the abundances calculated for C_7H_4 and C_6H_3N with the values observed in TMC-1. It is seen that peak calculated abundances, reached between 10^5 yr and 10^6 yr, are, within one order of magnitude, in good agreement with the observed values.
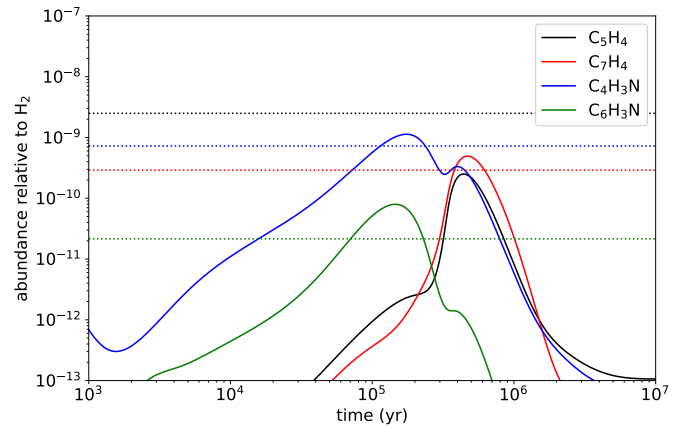
Fig. 3. Calculated fractional abundances of C_5H_4, C_7H_4, C_4H_3N, and C_6H_3N (allowing for various isomers) as a function of time. The horizontal dotted lines correspond to the abundances observed in TMC-1, where C_5H_4 includes CH_3C_4H and $CH_2CCHCCH$, C_7H_4 includes CH_3C_6H and CH_2CCHC_4H, C_4H_3N includes CH_3C_3N, CH_2CCHCN, and $HCCCH_2CN$, and C_6H_3N includes CH_3C_5N and CH_2CCHC_3N.

We note that the peak abundance is reached at different times for C_7H_4 and C_6H_3N. This is due to the different contribution of the neutral and ionic routes, both of which contribute to the formation of each species. The neutral route represented by reactions (1)–(4) is most efficient at times around $(4–5) \times 10^5$ yr

and this is the dominant route for C$_7$H$_4$. On the other hand, the ionic route, which involves as final step the dissociative recombination of C$_7$H$_5^+$ (to yield C$_7$H$_4$) and C$_6$H$_4$N$^+$ (to form C$_6$H$_3$N), is efficient at earlier times, in the range $(1–2)\times 10^5$ yr, and this pathway becomes dominant over the neutral route when forming C$_6$H$_3$N. Our chemical model is similar to that of Shingledecker et al. (2021) in that both explain the abundance derived for CH$_2$CCHC$_3$N in TMC-1 through gas-phase chemistry. There are however some differences. In our case two gas-phase routes contribute to the formation of CH$_2$CCHC$_3$N: (1) the neutral one based on the reaction of C$_3$N with CH$_3$CCH and CH$_2$CCH$_2$ and (2) the ionic one based on the dissociative recombination of C$_6$H$_4$N$^+$, and the resulting peak abundance of CH$_2$CCHC$_3$N is in the range between 10^{-11} and 10^{-10} relative to H$_2$. In the model of Shingledecker et al. (2021), CH$_2$CCHC$_3$N is mainly formed through the gas-phase neutral route and the peak abundance is substantially higher, in the range between 10^{-9} and 10^{-8} relative to H$_2$, probably because these authors consider a C/O ratio higher than 1, whereas we adopted a C/O ratio of 0.55.

The column densities of CH$_3$C$_6$H and CH$_3$C$_5$N in TMC-1 are 7×10^{11} cm^{-2} and 9.5×10^{10} cm^{-2}, respectively (see Appendix C). This implies that the abundance ratio CH$_3$C$_6$H/CH$_2$CCHC$_4$H is 0.32, which is somewhat lower than that of the smaller analogue system CH$_3$C$_4$H/CH$_2$CCHCCH = 1.1 (Cernicharo et al. 2021e). On the other hand, the abundance ratio CH$_3$C$_5$N/CH$_2$CCHC$_3$N is 0.79, which is similar to the abundance ratio of the smaller analogue system CH$_3$C$_3$N/CH$_2$CCHCN = 0.64 (Marcelino et al. 2021). If most of the synthesis of C$_7$H$_4$ and C$_6$H$_3$N isomers is carried out by reactions (1)–(4), this implies that CH$_2$CCHC$_4$H would be favoured over CH$_3$C$_6$H in reactions (1)–(2), while CH$_3$C$_5$N and CH$_2$CCHC$_3$N would be produced with similar branching ratios in reactions (3)–(4). Moreover, given that in the analogue smaller system C$_4$H$_3$N, three different isomers (CH$_3$C$_3$N, CH$_2$CCHCN, and HCCCH$_2$CN) have been detected in TMC-1 with similar abundances (Marcelino et al. 2021), it would not be surprising to find that the isomer HCCCH$_2$C$_3$N would also be detected in TMC-1.

5. Conclusions

We report the first detection in space of CH$_2$CCHC$_4$H, towards the cold dark cloud TMC-1. The CH$_2$CCHC$_3$N molecule was also detected in a robust way, which allows for its frequencies and rotational constants to be presented for the first time. We observed a total of 20 rotational transitions, from $J = 17$ to 24 and $K_a \leq 3$, using the Yebes 40 m telescope. The frequencies predicted for these two species from laboratory data are rather accurate when compared with those derived from astronomical observations. The rotational temperature for both species is 9.0 ± 0.5 K and the derived column densities are $(2.2\pm 0.2)\times 10^{12}$ cm^{-2}

for CH$_2$CCHC$_4$H and $(1.2\pm 0.15)\times 10^{11}$ cm^{-2} for CH$_2$CCHC$_3$N. These values give an abundance ratio between CH$_2$CCHC$_4$H and CH$_2$CCHC$_3$N of 18 ± 4. The observed abundances of the C$_7$H$_4$ and C$_6$H$_3$N isomeric families are reasonably well reproduced by a gas-phase chemical model in which the main formation pathways involve dissociative recombination of the precursor ions C$_7$H$_5^+$ and C$_6$H$_4^+$ and neutral-neutral reactions involving the C$_4$H and CN reactions with CH$_3$CCH and CH$_2$CCH$_2$.

References

Agúndez, M., & Wakelam, V. 2013, Chem. Rev., 113, 8710
Agúndez, M., Cabezas, C., Tercero, B., et al. 2021, A&A, 647, L10
Agúndez, M., Marcelino, N., Cabezas, C., et al. 2022, A&A, 657, A96
Berteloite, C., Le Picard, S., Balucani, N., et al. 2010, PCCP, 12, 3677
Cabezas, C., Tercero, B., Agúndez, M., et al. 2021, A&A, 650, L9
Cernicharo, J. 1985, Internal IRAM report (Granada: IRAM)
Cernicharo, J. 2012, in ECLA 2011: Proc. of the European Conference on Laboratory Astrophysics, eds. C. Stehl, C. Joblin, & L. d'Hendecourt (Cambridge: Cambridge Univ. Press), EAS Pub. Ser., 2012, 251
Cernicharo, J., & Guélin, M. 1987, A&A, 176, 299
Cernicharo, J., Agúndez, M., Kaiser, R., et al. 2021a, A&A, 652, L9
Cernicharo, J., Agúndez, M., Cabezas, C., et al. 2021b, A&A, 649, L15
Cernicharo, J., Agúndez, M., Kaiser, R. I., et al. 2021c, A&A, 655, L1
Cernicharo, J., Agúndez, M., Cabezas, C., et al. 2021d, A&A, 647, L2
Cernicharo, J., Cabezas, C., Agúndez, M., et al. 2021e, A&A, 647, L3
Cernicharo, J., Agúndez, M., Kaiser, R. I., et al. 2021f, A&A, 655, L1
Fossé, D., Cernicharo, J., Gerin, M., & Cox, P. 2001, ApJ, 552, 168
Fournier, M. 2014, Ph.D. Thesis, Université de Rennes, France
Kaifu, N., Ohishi, M., Kawaguchi, K., et al. 2004, PASJ, 56, 69
Lee, K. L. K., Changala, P. B., Loomis, R. A., et al. 2021, ApJ, 910, L2
Loison, J.-C., Agúndez, M., Wakelam, V., et al. 2017, MNRAS, 470, 4075
Marcelino, N., Tercero, B., Agúndez, M., & Cernicharo, J. 2021, A&A, 646, L9
McCarthy, M. C., Lee, K. L. K., Porterfield, J. P., et al. 2020, J. Phys. Chem. A, 124, 5170
McCarthy, M. C., Lee, K. L. K., Loomis, R. A., et al. 2021, Nat. Astron., 5, 176
McElroy, D., Walsh, C., Markwick, A. J., et al. 2013, A&A, 550, A36
McGuire, B. A., Burkhardt, A. M., Kalenskii, S., et al. 2018, Science, 359, 202
McGuire, B. A., Loomis, R. A., Burkhardt, A. M., et al. 2021, Science, 371, 1265
Müller, H. S. P., Schlöder, F., Stutzki, J., & Winnewisser, G. 2005, J. Mol. Struct., 742, 215
Pardo, J. R., Cernicharo, J., & Serabyn, E. 2001, IEEE Trans. Antennas Propag., 49, 12
Pickett, H. M., & Boyd, T. L. 1978, Chem. Phys. Lett., 58, 446
Pickett, H. M., Poynter, R. L., Cohen, E. A., et al. 1998, J. Quant. Spectrosc. Radiat. Trans., 60, 883
Remijan, A. J., Hollis, J. M., Snyder, L. E., et al. 2006, ApJ, 643, L37
Shingledecker, C. N., Lee, K. L. K., Wandishin, J. T., et al. 2021, A&A, 652, L12
Snyder, L. E., Hollis, J. M., Jewell, P. R., et al. 2006, ApJ, 647, 412
Tercero, F., López-Pérez, J. A., Gallego, J. D., et al. 2021, A&A, 645, A37

Appendix A: Observed line parameters

The line parameters for the different molecules studied in this work were obtained by fitting a Gaussian line profile to the observed data. A window of $\pm$ 15 km s^{-1} around the v_{LSR} of the source was considered for each transition. The derived line parameters for all the molecular species studied in this work are given in Table A.1. The observed lines of CH$_2$CCHC$_4$H are shown on Fig. 1. Selected lines of CH$_2$CCHC$_3$N are shown on Fig. 2. All lines of both species are weak, with many of them blended with other features. Nevertheless, for most of these blended lines, it is still possible to derive reliable line parameters. It is worth noting that at this level of sensitivity any stacking procedure is not at all recommended due to the forest of weak unknown features. For CH$_2$CCHC$_3$N, we explored lines with K_a=3, but only three of them were detected. These lines involve high energy levels and exhibit intrinsic line strengths weaker than those with K_a=0, 1, and 2. This species also demonstrate a hyperfine structure due to the nitrogen nuclear spin. None of the hyperfine structures are resolved as the splitting is predicted to be of ~5 kHz for K_a=0 and 1 and around 10 kHz for K_a=2; this is much lower than our spectral resolution of 38.1 kHz. However, the observed linewidths for many of the lines of this species indicate some broadening. For the modelling of the emerging spectrum of this molecule, we used predictions taken into account the hyperfine splitting.

Table A.1. Observed line parameters for the species studied in this work.

Transition[1]	ν_{rest} [a] (MHz)	$\int T_A^* dv$ [b] (mK km s^{-1})	Δv [c] (km s^{-1})	T_A^* [d] (mK)	Notes
		CH$_2$CCHC$_4$H[1]			
$17_{0,17} - 16_{0,16}$	31281.977±0.015	0.36±0.10	0.68±0.15	0.50±0.12	
$17_{2,16} - 16_{2,15}$	31369.493±0.002			≤0.45	A
$17_{2,15} - 16_{2,14}$	31470.108±0.015	0.35±0.11	0.54±0.20	0.60±0.17	B
$17_{1,16} - 16_{1,15}$	31778.167±0.030	0.47±0.09	0.66±0.00	0.66±0.14	C
$18_{1,18} - 17_{1,17}$	32754.991±0.015	0.59±0.16	1.27±0.37	0.44±0.14	
$18_{0,18} - 17_{0,17}$	33109.190±0.002				A
$18_{2,17} - 17_{2,16}$	33212.230±0.020	0.30±0.08	0.83±0.24	0.34±0.11	D
$18_{2,16} - 17_{2,15}$	33331.250±0.015	0.54±0.15	0.74±0.14	0.68±0.11	
$18_{1,17} - 17_{1,16}$	33643.419±0.015	0.48±0.11	0.64±0.16	0.71±0.13	
$19_{1,19} - 18_{1,18}$	34571.094±0.015	0.40±0.08	0.56±0.13	0.67±0.14	
$19_{0,19} - 18_{0,18}$	34934.337±0.015	0.35±0.10	0.54±0.19	0.59±0.14	
$19_{2,18} - 18_{2,17}$	35054.486±0.030	0.41±0.10	0.75±0.00	0.50±0.14	E
$19_{2,17} - 18_{2,16}$	35193.985±0.004			≤0.44	A
$19_{1,18} - 18_{1,17}$	35507.943±0.003				F
$20_{1,20} - 19_{1,19}$	36386.699±0.015	0.26±0.09	0.55±0.12	0.45±0.11	
$20_{0,20} - 19_{0,19}$	36757.421±0.015	0.64±0.13	0.96±0.25	0.63±0.14	
$20_{2,19} - 19_{2,18}$	36896.323±0.020	0.25±0.08	0.55±0.22	0.48±0.14	B
$20_{2,18} - 19_{2,17}$	37058.291±0.015	0.43±0.09	0.59±0.16	0.70±0.15	
$20_{1,19} - 19_{1,18}$	37371.695±0.004			≤0.42	A
$21_{1,21} - 20_{1,20}$	38201.714±0.015	0.29±0.08	0.72±0.23	0.38±0.12	
$21_{0,21} - 20_{0,20}$	38578.311±0.015	0.19±0.06	0.37±0.14	0.48±0.13	
$21_{2,20} - 20_{2,19}$	38737.658±0.015	0.14±0.05	0.29±0.15	0.42±0.12	
$21_{2,19} - 20_{2,18}$	38924.186±0.015	0.16±0.06	0.30±0.17	0.50±0.13	
$21_{1,20} - 20_{1,19}$	39234.610±0.005			≤1.2	A,G
$22_{1,22} - 21_{1,21}$	40016.225±0.015	0.38±0.09	0.49±0.15	0.73±0.15	
$22_{0,22} - 21_{0,21}$	40397.015±0.015	0.29±0.08	0.64±0.27	0.42±0.16	
$22_{1,21} - 21_{1,20}$	41096.635±0.006			≤0.55	A
$23_{1,23} - 22_{1,22}$	41830.115±0.006				H
$23_{0,23} - 22_{0,22}$	42213.561±0.004			≤0.48	A
$23_{1,22} - 22_{1,21}$	42957.710±0.015	0.34±0.12	0.61±0.20	0.51±0.18	
$24_{0,24} - 23_{0,23}$	44027.907±0.005			≤0.60	A,I

Table A.1. continued.

Transition[1]	ν_{rest} [a] (MHz)	$\int T_A^* dv$ [b] (mK km s^{-1})	Δv [c] (km s^{-1})	T_A^* [d] (mK)	Notes
		CH$_2$CCHC$_3$N[1]			
$17_{1,17} - 16_{1,16}$	31112.574±0.015	0.75±0.15	0.77±0.00	0.92±0.12	C
$17_{0,17} - 16_{0,16}$	31463.463±0.015	0.99±0.21	1.17±0.35	0.80±0.12	
$17_{2,16} - 16_{2,15}$	31558.376±0.015	0.44±0.12	0.52±0.18	0.76±0.18	
$17_{3,15} - 16_{3,14}$	31593.484±0.020	0.38±0.11	0.65±0.19	0.55±0.18	
$17_{3,14} - 16_{3,13}$	31596.159±0.016			≤0.54	
$17_{2,15} - 16_{2,14}$	31667.997±0.015	0.44±0.11	0.73±0.18	0.56±0.14	
$17_{1,16} - 16_{1,15}$	31980.224±0.010	0.86±0.09	0.81±0.10	0.99±0.13	
$18_{1,18} - 17_{1,17}$	32939.203±0.010	0.57±0.08	0.78±0.12	0.68±0.12	
$18_{0,18} - 17_{0,17}$	33300.280±0.010	0.97±0.11	0.92±0.13	0.99±0.13	
$18_{2,17} - 17_{2,16}$	33411.994±0.015	0.52±0.16	1.12±0.29	0.51±0.13	
$18_{3,16} - 17_{3,15}$	33453.015±0.017			≤0.40	I
$18_{3,15} - 17_{3,14}$	33456.519±0.016				D
$18_{2,16} - 17_{2,15}$	33541.670±0.015	0.53±0.12	0.88±0.27	0.57±0.13	
$18_{1,17} - 17_{1,16}$	33857.014±0.010	0.59±0.09	0.78±0.13	0.72±0.12	
$19_{1,19} - 18_{1,18}$	34765.294±0.015	0.53±0.10	0.69±0.14	0.72±0.14	
$19_{0,19} - 18_{0,18}$	35134.847±0.020	0.35±0.11	0.50±0.16	0.66±0.16	
$19_{2,18} - 18_{2,17}$	35265.143±0.020	0.54±0.06	0.60±0.00	0.85±0.12	C
$19_{3,17} - 18_{3,16}$	35312.608±0.015	0.36±0.10	0.65±0.20	0.51±0.15	
$19_{3,16} - 18_{3,15}$	35317.258±0.020	0.21±0.08	0.67±0.23	0.34±0.14	
$19_{2,17} - 18_{2,16}$	35416.968±0.020	0.24±0.07	0.61±0.24	0.36±0.11	
$19_{1,18} - 18_{1,17}$	35733.011±0.020	0.41±0.13	0.63±0.25	0.61±0.17	
$20_{1,20} - 19_{1,19}$	36590.744±0.010	0.55±0.11	0.90±0.17	0.57±0.14	
$20_{0,20} - 19_{0,19}$	36967.205±0.015	0.27±0.07	0.61±0.16	0.42±0.12	
$20_{2,19} - 19_{2,18}$	37117.811±0.010	0.44±0.08	0.65±0.11	0.64±0.12	
$20_{2,18} - 19_{2,17}$	37293.956±0.020	0.55±0.19	0.93±0.33	0.56±0.13	B
$21_{2,20} - 20_{2,19}$	38969.920±0.007			≤0.42	A
$21_{2,19} - 20_{2,18}$	39172.697±0.008			≤0.45	A
$22_{2,21} - 21_{2,20}$	40821.522±0.010	0.47±0.12	0.65±0.18	0.69±0.18	
$22_{2,20} - 21_{2,19}$	41053.129±0.020	0.28±0.07	0.60±0.16	0.44±0.12	
$22_{1,21} - 21_{1,20}$	41355.602±0.020	0.20±0.08	0.38±0.13	0.66±0.18	
$23_{1,23} - 22_{1,22}$	42063.663±0.015	0.35±0.08	0.61±0.19	0.53±0.12	
$23_{0,23} - 22_{0,22}$	42450.325±0.020	0.38±0.09	0.54±0.18	0.65±0.18	
$23_{2,22} - 22_{2,21}$	42672.553±0.020	0.21±0.08	0.40±0.24	0.49±0.18	
$23_{2,21} - 22_{2,20}$				≤0.51	A
$23_{1,22} - 22_{1,21}$	43227.824±0.005				D

Notes. [1]Quantum numbers are $J'_{K'_a, K'_c} - J_{K_a, K_c}$. [a]Observed frequency of the transition assuming a LSR velocity of 5.83 km s^{-1}. See text for the laboratory data used for initial frequency predictions of each molecular species. For lines for which only upper limits are given, their frequencies correspond to the predictions obtained from a fit to the laboratory plus space lines (see Table B.1). [b]Integrated line intensity in mK km s^{-1}. [c]Linewidth at half intensity derived by fitting a Gaussian function to the observed line profile (in km s^{-1}). [d]Antenna temperature in milli Kelvin. [A]Upper limit corresponds to 3σ. [B]The line is partially blended but still possible to derive line parameters. [C]This line is blended with an U line. Line width has been fixed. [D]This line is blended with a feature stronger than expected. It is, more likely, an unknown line. [E]This line is blended with a transition of H$_2$C$_4$N. [F]This line is heavily blended a transition of C^{13}CCCCH. Line parameters can not be derived. [G]The frequency of this transition of CH$_2$CCHC$_4$H is within a poor sensitivity zone of the receiver. [H]This line is blended with a broad 1 mK unknown line. [I]A 3σ feature do appears just at the expected frequency of this transition.

Appendix B: Improved rotational constants for CH$_2$CCHC$_4$H and CH$_2$CCHC$_3$N

We merged the laboratory lines of CH$_2$CCHC$_4$H and CH$_2$CCHC$_3$N with those observed in TMC-1 with the QUIJOTE line survey to obtain improved rotational and distortion constants for both species. The results for CH$_2$CCHC$_4$H are given in Table B.1. The predictions from the laboratory data were rather accurate, with deviations between our observed frequencies of a few kHz (see Table B.3). Some lines show differences of up to 25 kHz which is at most 1.5-2 times the accuracy of the observed

frequencies in TMC-1 as the signal-to-noise ratio (S/N) of the observations is limited to ~4-5. As a consequence, the derived constants for this species from the merged fit are practically identical to those obtained from the laboratory data alone. However, the uncertainty of the constants is significantly improved.

The results for CH$_2$CCHC$_3$N are given in Table B.2. The new constants are very similar to the laboratory data, with most of the differences being at frequencies below 3 kHz (see Table B.4) and presenting a maximum deviation of 47 kHz. As in the previous case, the values of the constants obtained are in good agreement with the laboratory data.

Table B.1. Improved rotational and distortion constants for CH_2CCHC_4H.

Constant (MHz)	Laboratory[1]	Lab + TMC-1[2]
A	15654.01571(87)	15654.01571(97)
B	947.90683(11)	947.906800(92)
C	898.29939(10)	898.299386(82)
$D_J \times 10^4$	1.4692(15)	1.4686(10)
$D_{JK} \times 10^2$	-2.48883(88)	-2.48885(93)
$d_J \times 10^5$	3.100(20)	3.097(14)
J_{max}	13	23
$K_{a,max}$	2	2
N_{lines}	45	67
σ (kHz)	1.7	9.3
ν_{max} (MHz)	24310	42957

Notes. [1]Rotational and distortion constants derived from a fit to the laboratory data of McCarthy et al. (2020). [2]Merged rotational and distortion constants from a fit to the laboratory and TMC-1 frequencies.

Table B.2. Improved rotational and distortion constants for CH_2CCHC_3N.

Constant (MHz)	Laboratory[1]	Lab + TMC-1[2]
A	15351.89314(36)	15351.89321(41)
B	954.343246(105)	954.343014(70)
C	903.075581(88)	903.075751(62)
$D_J \times 10^4$	1.53425(187)	1.53243(73)
$D_{JK} \times 10^2$	-24.1218(75)	-24.1204(78)
$d_J \times 10^5$	3.2427(274)	3.1674(92)
χ_{aa}	-3.77238(147)	-3.77234(167)
χ_{bb}	1.74588(148)	1.74567(168)
J_{max}	15	23
$K_{a,max}$	2	3
N_{lines}	100	134
σ (kHz)	1.7	8.9
ν_{max} (MHz)	27783	43227

Notes. [1]Rotational and distortion constants kindly provided by M. McCarthy. [2]Merged rotational and distortion constants from a fit to the laboratory and TMC-1 frequencies.

Table B.3. Observed frequencies of CH_2CCHC_4H

Transition $J'_{K'_a,K'_c} - J_{K_a,K_c}$	ν_{obs} (MHz)	$\nu_{obs} - \nu_{cal}$ (kHz)	Ref
$4_{1,4} - 3_{1,3}$	7285.5300±0.002	0.60	1
$4_{0,4} - 3_{0,3}$	7383.5340±0.002	-0.48	1
$4_{1,3} - 3_{1,2}$	7483.9430±0.002	0.98	1
$5_{1,5} - 4_{1,4}$	9106.6580±0.002	0.61	1
$5_{0,5} - 4_{0,4}$	9228.4530±0.002	0.47	1
$5_{1,4} - 4_{1,3}$	9354.6610±0.002	1.66	1
$6_{1,6} - 5_{1,5}$	10927.6180±0.002	1.05	1
$6_{0,6} - 5_{0,5}$	11072.7280±0.002	0.53	1
$6_{1,5} - 5_{1,4}$	11225.1980±0.002	1.15	1
$7_{1,7} - 6_{1,6}$	12748.3760±0.002	0.46	1

Table B.3. continued.

Transition $J'_{K'_a,K'_c} - J_{K_a,K_c}$	ν_{obs} (MHz)	$\nu_{obs} - \nu_{cal}$ (kHz)	Ref
$7_{0,7} - 6_{0,6}$	12916.2310±0.002	-0.52	1
$7_{1,6} - 6_{1,5}$	13095.5180±0.002	0.44	1
$8_{1,8} - 7_{1,7}$	14568.9020±0.002	0.73	1
$8_{0,8} - 7_{0,7}$	14758.8370±0.002	-0.64	1
$8_{1,7} - 7_{1,6}$	14965.5850±0.002	1.06	1
$9_{1,9} - 8_{1,8}$	16389.1630±0.002	0.08	1
$9_{0,9} - 8_{0,8}$	16600.4190±0.002	-0.92	1
$9_{1,8} - 8_{1,7}$	16835.3570±0.002	-0.77	1
$10_{1,10} - 9_{1,9}$	18209.1310±0.002	0.88	1
$10_{0,10} - 9_{0,9}$	18440.8540±0.002	-0.02	1
$11_{0,11} - 10_{0,10}$	20280.0170±0.002	-0.81	1
$11_{1,10} - 10_{1,9}$	20573.8720±0.002	0.81	1
$12_{1,12} - 11_{1,11}$	21848.0660±0.002	1.66	1
$12_{0,12} - 11_{0,11}$	22117.7910±0.002	-1.06	1
$12_{1,11} - 11_{1,10}$	22442.5300±0.002	-0.23	1
$13_{1,13} - 12_{1,12}$	23666.9750±0.002	-0.53	1
$13_{0,13} - 12_{0,12}$	23954.0590±0.002	-2.32	1
$13_{1,12} - 12_{1,11}$	24310.7360±0.002	0.52	1
$5_{2,4} - 4_{2,3}$	9231.6750±0.002	0.32	1
$5_{2,3} - 4_{2,2}$	9234.1780±0.002	-1.65	1
$7_{2,6} - 6_{2,5}$	12923.6610±0.002	-0.54	1
$6_{2,5} - 5_{2,4}$	11077.7410±0.002	-0.25	1
$6_{2,4} - 5_{2,3}$	11082.1220±0.002	-2.00	1
$7_{2,5} - 6_{2,4}$	12930.6710±0.002	-0.79	1
$8_{2,7} - 7_{2,6}$	14769.4100±0.002	-1.21	1
$8_{2,6} - 7_{2,5}$	14779.9210±0.002	-1.20	1
$9_{2,8} - 8_{2,7}$	16614.9660±0.002	0.00	1
$9_{2,7} - 8_{2,6}$	16629.9720±0.002	-1.31	1
$10_{2,9} - 9_{2,8}$	18460.3080±0.002	6.34	1
$10_{2,8} - 9_{2,7}$	18480.9200±0.002	-1.63	1
$1_{1,0} - 1_{0,1}$	14755.7680±0.002	2.02	1
$1_{1,1} - 0_{0,0}$	16552.3630±0.002	-1.41	1
$2_{1,2} - 1_{0,1}$	18349.0590±0.002	-0.61	1
$11_{2,10} - 10_{2,9}$	20305.3950±0.002	0.97	1
$11_{2,9} - 10_{2,8}$	20332.8600±0.002	-1.50	1
$17_{0,17} - 16_{0,16}$	31281.9770±0.015	7.13	2
$17_{2,15} - 16_{2,14}$	31470.1080±0.015	-14.60	2
$17_{1,16} - 16_{1,15}$	31778.1670±0.030	25.67	2
$18_{1,18} - 17_{1,17}$	32754.9910±0.015	26.74	2
$18_{2,17} - 17_{2,16}$	33212.2300±0.020	18.16	2
$18_{2,16} - 17_{2,15}$	33331.2500±0.015	-27.35	2
$18_{1,17} - 17_{1,16}$	33643.4190±0.015	11.01	2
$19_{1,19} - 18_{1,18}$	34571.0940±0.015	0.50	2
$19_{0,19} - 18_{0,18}$	34934.3370±0.015	-17.72	2
$19_{2,18} - 18_{2,17}$	35054.4860±0.030	-10.68	2
$20_{1,20} - 19_{1,19}$	36386.6990±0.015	10.54	2
$20_{0,20} - 19_{0,19}$	36757.4210±0.015	12.62	2
$20_{2,19} - 19_{2,18}$	36896.3230±0.020	-01.70	2
$20_{2,18} - 19_{2,17}$	37058.2910±0.015	13.42	2
$21_{1,21} - 20_{1,20}$	38201.7140±0.015	-19.11	2
$21_{0,21} - 20_{0,20}$	38578.3110±0.015	1.88	2
$21_{2,20} - 20_{2,19}$	38737.6580±0.015	-14.91	2
$21_{2,19} - 20_{2,18}$	38924.1860±0.015	21.35	2
$22_{1,22} - 21_{1,21}$	40016.2250±0.015	11.95	2
$22_{0,22} - 21_{0,21}$	40397.0150±0.015	-15.16	2
$23_{1,22} - 22_{1,21}$	42957.7100±0.015	0.24	2

Notes. [1]Laboratory frequencies from McCarthy et al. (2020). [2]TMC-1 frequencies from Table A.1.

Table B.4. Observed frequencies of CH_2CCHC_3N

Transition $J'_{K'_a, K'_c} - J_{K_a, K_c}$	F'	F	ν_{obs} (MHz)	$\nu_{obs} - \nu_{cal}$ (kHz)	Ref
$4_{0,4} - 3_{0,3}$	4	4	7427.010±0.002	-1.41	1
$4_{0,4} - 3_{0,3}$	3	2	7428.189±0.002	0.36	1
$4_{0,4} - 3_{0,3}$	4	3	7428.270±0.002	0.86	1
$4_{0,4} - 3_{0,3}$	5	4	7428.298±0.002	-0.08	1
$4_{0,4} - 3_{0,3}$	3	3	7429.886±0.002	-0.94	1
$6_{0,6} - 5_{0,5}$	5	4	11139.572±0.002	0.94	1
$6_{0,6} - 5_{0,5}$	6	5	11139.598±0.002	-1.09	1
$6_{0,6} - 5_{0,5}$	7	6	11139.615±0.002	0.87	1
$7_{1,7} - 6_{1,6}$	7	6	12820.872±0.002	0.78	1
$7_{1,7} - 6_{1,6}$	6	5	12820.882±0.002	2.54	1
$7_{1,7} - 6_{1,6}$	8	7	12820.907±0.002	1.14	1
$7_{0,7} - 6_{0,6}$	6	5	12994.054±0.002	-0.82	1
$7_{0,7} - 6_{0,6}$	7	6	12994.073±0.002	-0.97	1
$7_{0,7} - 6_{0,6}$	8	7	12994.086±0.002	0.32	1
$7_{1,6} - 6_{1,5}$	7	6	13179.626±0.002	-0.47	1
$7_{1,6} - 6_{1,5}$	6	5	13179.638±0.002	1.81	1
$7_{1,6} - 6_{1,5}$	8	7	13179.660±0.002	-0.30	1
$1_{1,0} - 1_{0,1}$	1	0	14447.486±0.002	0.45	1
$1_{1,0} - 1_{0,1}$	2	2	14448.578±0.002	2.41	1
$1_{1,0} - 1_{0,1}$	0	1	14448.796±0.002	0.68	1
$1_{1,0} - 1_{0,1}$	1	2	14449.184±0.002	0.69	1
$1_{1,0} - 1_{0,1}$	2	1	14449.709±0.002	1.92	1
$1_{1,0} - 1_{0,1}$	1	1	14450.314±0.002	-0.80	1
$2_{1,1} - 2_{0,2}$	2	1	14498.986±0.002	0.98	1
$2_{1,1} - 2_{0,2}$	1	1	14499.859±0.002	0.58	1
$2_{1,1} - 2_{0,2}$	3	3	14500.222±0.002	1.84	1
$2_{1,1} - 2_{0,2}$	2	2	14500.872±0.002	0.25	1
$2_{1,1} - 2_{0,2}$	1	2	14501.745±0.002	-0.15	1
$3_{1,2} - 3_{0,3}$	3	4	14576.883±0.002	1.29	1
$3_{1,2} - 3_{0,3}$	4	4	14577.779±0.002	1.12	1
$3_{1,2} - 3_{0,3}$	3	3	14578.140±0.002	0.56	1
$8_{0,8} - 7_{0,7}$	7	6	14847.557±0.002	-0.02	1
$8_{0,8} - 7_{0,7}$	8	7	14847.570±0.002	-0.80	1
$8_{0,8} - 7_{0,7}$	9	8	14847.582±0.002	1.74	1
$8_{2,7} - 7_{2,6}$	8	7	14858.869±0.002	3.38	1
$8_{2,7} - 7_{2,6}$	7	6	14858.926±0.002	-0.18	1
$8_{2,7} - 7_{2,6}$	9	8	14858.939±0.002	2.56	1
$8_{2,6} - 7_{2,5}$	8	7	14870.330±0.002	-0.99	1
$8_{2,6} - 7_{2,5}$	7	6	14870.386±0.002	-4.81	1
$8_{2,6} - 7_{2,5}$	9	8	14870.398±0.002	-3.11	1
$8_{1,7} - 7_{1,6}$	8	7	15061.654±0.002	-0.55	1
$8_{1,7} - 7_{1,6}$	7	6	15061.661±0.002	1.50	1
$8_{1,7} - 7_{1,6}$	9	8	15061.678±0.002	-0.66	1
$1_{1,1} - 0_{0,0}$	0	1	16254.142±0.002	-2.20	1
$1_{1,1} - 0_{0,0}$	2	1	16254.929±0.002	-0.51	1
$1_{1,1} - 0_{0,0}$	1	1	16255.451±0.002	-1.90	1
$9_{1,9} - 8_{1,8}$	8	7	16482.250±0.002	1.43	1
$9_{1,9} - 8_{1,8}$	10	9	16482.268±0.002	2.58	1
$9_{0,9} - 8_{0,8}$	8	7	16699.940±0.002	-2.40	1
$9_{0,9} - 8_{0,8}$	9	8	16699.952±0.002	-0.67	1
$9_{0,9} - 8_{0,8}$	10	9	16699.962±0.002	1.45	1
$9_{2,8} - 8_{2,7}$	9	8	16715.570±0.002	0.91	1
$9_{2,8} - 8_{2,7}$	8	7	16715.609±0.002	-0.89	1
$9_{2,8} - 8_{2,7}$	10	9	16715.627±0.002	6.96	1
$9_{2,7} - 8_{2,6}$	9	8	16731.938±0.002	-0.20	1
$9_{2,7} - 8_{2,6}$	8	7	16731.977±0.002	-1.17	1
$9_{2,7} - 8_{2,6}$	10	9	16731.988±0.002	-0.36	1

Table B.4. continued.

Transition $J'_{K'_a, K'_c} - J_{K_a, K_c}$	F'	F	ν_{obs} (MHz)	$\nu_{obs} - \nu_{cal}$ (kHz)	Ref
$9_{1,8} - 8_{1,7}$	9	8	16943.364±0.004	1.49	1
$9_{1,8} - 8_{1,7}$	8	7	16943.364±0.004	-0.98	1
$9_{1,8} - 8_{1,7}$	10	9	16943.382±0.002	1.53	1
$2_{1,2} - 1_{0,1}$	1	0	18059.882±0.002	-0.45	1
$2_{1,2} - 1_{0,1}$	2	2	18060.566±0.002	-0.32	1
$2_{1,2} - 1_{0,1}$	2	1	18061.697±0.002	-0.81	1
$2_{1,2} - 1_{0,1}$	1	1	18062.713±0.002	1.29	1
$10_{0,10} - 9_{0,9}$	9	8	18551.073±0.002	-3.71	1
$10_{0,10} - 9_{0,9}$	10	9	18551.085±0.002	0.45	1
$10_{0,10} - 9_{0,9}$	11	10	18551.093±0.002	1.71	1
$10_{2,9} - 9_{2,8}$	10	9	18572.031±0.002	0.86	1
$10_{2,9} - 9_{2,8}$	9	8	18572.058±0.002	-0.79	1
$10_{2,9} - 9_{2,8}$	11	10	18572.070±0.002	1.83	1
$10_{2,8} - 9_{2,7}$	10	9	18594.518±0.002	-1.72	1
$10_{2,8} - 9_{2,7}$	9	8	18594.543±0.002	-4.45	1
$10_{2,8} - 9_{2,7}$	11	10	18594.557±0.002	0.12	1
$10_{1,9} - 9_{1,8}$	10	9	18824.709±0.004	0.14	1
$10_{1,9} - 9_{1,8}$	9	8	18824.709±0.004	-0.98	1
$10_{1,9} - 9_{1,8}$	11	10	18824.725±0.002	2.26	1
$3_{1,3} - 2_{0,2}$	2	1	19841.616±0.002	-1.87	1
$3_{1,3} - 2_{0,2}$	4	3	19841.943±0.002	-2.18	1
$3_{1,3} - 2_{0,2}$	3	2	19842.165±0.002	-2.88	1
$11_{1,11} - 0_{1,10}$	11	10	20142.342±0.002	1.49	1
$11_{1,11} - 0_{1,10}$	10	9	20142.342±0.002	1.68	1
$11_{1,11} - 0_{1,10}$	12	11	20142.356±0.002	4.12	1
$11_{0,11} - 0_{0,10}$	10	9	20400.825±0.002	-2.97	1
$11_{0,11} - 0_{0,10}$	11	10	20400.833±0.002	-1.06	1
$11_{0,11} - 0_{0,10}$	12	11	20400.841±0.002	1.05	1
$11_{1,10} - 0_{1,9}$	11	10	20705.648±0.004	-2.66	1
$11_{1,10} - 0_{1,9}$	10	9	20705.648±0.004	-3.02	1
$11_{1,10} - 0_{1,9}$	12	11	20705.662±0.002	0.31	1
$12_{0,12} - 1_{0,11}$	11	10	22249.065±0.002	-2.53	1
$12_{0,12} - 1_{0,11}$	12	11	22249.071±0.002	-1.30	1
$12_{0,12} - 1_{0,11}$	13	12	22249.077±0.002	-0.54	1
$13_{0,13} - 2_{0,12}$	13	12	24095.674±0.004	-0.89	1
$13_{0,13} - 2_{0,12}$	14	13	24095.674±0.004	-5.64	1
$13_{0,13} - 2_{0,12}$	12	11	24095.674±0.004	2.86	1
$14_{0,14} - 3_{0,13}$	14	13	25940.525±0.004	1.84	1
$14_{0,14} - 3_{0,13}$	15	14	25940.525±0.004	-2.52	1
$14_{0,14} - 3_{0,13}$	13	12	25940.525±0.004	4.78	1
$15_{0,15} - 4_{0,14}$	14	13	27783.508±0.004	4.79	1
$15_{0,15} - 4_{0,14}$	15	14	27783.508±0.004	2.51	1
$15_{0,15} - 4_{0,14}$	16	15	27783.508±0.004	-1.55	1
$17_{1,17} - 6_{1,16}$			31112.574±0.015	7.24	2
$17_{0,17} - 6_{0,16}$			31463.463±0.015	-10.49	2
$17_{2,16} - 6_{2,15}$			31558.376±0.015	-6.50	2
$17_{3,15} - 6_{3,14}$			31593.484±0.020	-47.78	2
$17_{3,14} - 6_{3,13}$			31596.159±0.016	-4.06	2
$17_{2,15} - 6_{2,14}$			31667.997±0.015	2.59	2
$17_{1,16} - 6_{1,15}$			31980.224±0.010	-9.75	2
$18_{1,18} - 7_{1,17}$			32939.203±0.010	6.65	2
$18_{0,18} - 7_{0,17}$			33300.280±0.010	-0.89	2
$18_{2,17} - 7_{2,16}$			33411.994±0.015	-3.94	2
$18_{3,16} - 7_{3,15}$			33453.015±0.017	-3.46	2
$18_{3,15} - 7_{3,14}$			33456.519±0.016	-4.13	2
$18_{2,16} - 7_{2,15}$			33541.670±0.015	24.42	2
$18_{1,17} - 7_{1,16}$			33857.014±0.010	-10.27	2

Table B.4. continued.

Transition $J'_{K'_a,K'_c} - J_{K_a,K_c}$	F'	F	ν_{obs} (MHz)	$\nu_{obs} - \nu_{cal}$ (kHz)	Ref
$19_{1,19} - 8_{1,18}$			34765.294 ± 0.015	24.28	2
$19_{0,19} - 8_{0,18}$			35134.847 ± 0.020	-29.61	2
$19_{2,18} - 8_{2,17}$			35265.143 ± 0.020	-0.60	2
$19_{3,17} - 8_{3,16}$			35312.608 ± 0.015	-30.50	2
$19_{3,16} - 8_{3,15}$			35317.258 ± 0.020	25.06	2
$19_{2,17} - 8_{2,16}$			35416.968 ± 0.020	0.34	2
$19_{1,18} - 8_{1,17}$			35733.011 ± 0.020	-3.80	2
$20_{1,20} - 9_{1,19}$			36590.744 ± 0.010	-24.55	2
$20_{0,20} - 9_{0,19}$			36967.205 ± 0.015	-2.33	2
$20_{2,19} - 9_{2,18}$			37117.811 ± 0.010	16.58	2
$20_{2,18} - 9_{2,17}$			37293.956 ± 0.020	-27.72	2
$21_{2,20} - 0_{2,19}$			38969.920 ± 0.007	-5.53	2
$21_{2,19} - 0_{2,18}$			39172.697 ± 0.008	-3.45	2
$22_{2,21} - 1_{2,20}$			40821.522 ± 0.010	9.66	2
$22_{2,20} - 1_{2,19}$			41053.129 ± 0.020	22.05	2
$22_{1,21} - 1_{1,20}$			41355.602 ± 0.020	-2.82	2
$23_{1,23} - 2_{1,22}$			42063.663 ± 0.005	0.85	2
$23_{0,23} - 2_{0,22}$			42450.325 ± 0.005	-2.02	2
$23_{2,22} - 2_{2,21}$			42672.553 ± 0.020	22.45	2
$23_{1,22} - 2_{1,21}$			43227.824 ± 0.010	20.39	2

Notes. [1]Laboratory frequencies kindly provided by M. McCarthy. [2]TMC-1 frequencies from Table A.1.

Appendix C: Column densities of CH_3C_6H and CH_3C_5N

In order to obtain abundance ratios between the different ethynyl and cyanide derivatives of CH_2CCH_2 in a coherent and comprehensive way, we derived the column densities of CH_3C_6H (an isomer of CH_2CCHC_4H) and CH_3C_5N (an isomer of CH_2CCHC_3N) using the observed lines of these molecules within the QUIJOTE line survey. Both species have been previously detected towards TMC-1 (Remijan et al. 2006; Snyder et al. 2006). These authors reported a column density of 3.1×10^{12} cm^{-2} and a rotational temperature of 6K for CH_3C_6H, and N = 7.4×10^{11} cm^{-2} and T_{rot} = 4 K for CH_3C_5N.

In our data, we detected the rotational transitions J=20-19 up to J=31-30 for CH_3C_6H and CH_3C_5N (having very similar rotational constants). The K=0,1 components of all these lines (both species are symmetric rotors) are detected except the K=1 component of the J=30-29 transition of CH_3C_5N, which we explain as possibly due to an overlap with a negative feature produced in the folding of the frequency switching data. The observed transitions are shown on Fig. C.1 for CH_3C_6H and Fig. C.2 for CH_3C_5N. No K=2 lines are detected, which is reasonable taking into account the kinetic temperature of the cloud (10 K) and the high energy of the K=2 levels (from 38.9 for J_u=20 up to 57.3 K for J_u=30).

We derived the column densities and the rotational temperatures of CH_3C_6H and CH_3C_5N using a model line fitting procedure (see Section 3 in this work as well as Cernicharo et al. 2021d). We adopt a source of uniform brightness with a diameter of 80″ (Fossé et al. 2001, Cernicharo et al. in prep.) and a linewidth of 0.6 km s^{-1}. The best model for our CH_3C_6H lines provides N=$(7\pm0.7)\times10^{11}$ cm^{-2} and T_{rot} =9$\pm$0.5 K. The computed synthetic line profiles using these values are shown on Fig. C.1 as red lines. The derived rotational temperature and column density are rather different from those derived previously by Remijan et al. (2006). This difference is certainly due to the larger energy range covered by our data, which renders the line intensities very dependent on the rotational temperature. In Fig. C.1, we show in green the expected line profiles if we adopt the rotational temperature and column density derived by Remijan et al. (2006). The low-J transitions overestimate the observed intensities, while a reasonable agreement is found for $J_u \geq 27$. Using our derived parameters, we reproduce the intensities of the low-J transitions observed by Remijan et al. (2006) within a factor of 1.5.

For CH_3C_5N, we derived N=$(9.5\pm0.9)\times10^{10}$ cm^{-2} and T_{rot} = 9$\pm$0.5 K. The predicted synthetic lines for this species are shown on red in Fig C.2. These values are also different from those derived by Snyder et al. (2006), T_{rot} = 4 K and N=7.4×10^{11} cm^{-2}. With such a low value for the rotational temperature, it is impossible to reproduce the observed intensities of our lines. We show in green in Fig. C.2 the computed synthetic spectrum of CH_3C_5N adopting the parameters of Snyder et al. (2006). A good match is obtained for the transitions J=20-19 and J=21-20 but a clear underestimation of the intensity is observed for lines with higher J. Using our T_{rot} and column density for this species, we reproduce the intensities observed for the low-J transitions by Snyder et al. (2006) within a factor of 2.

Adopting a H_2 column density for TMC-1 of 10^{22} cm^{-2} (Cernicharo & Guélin 1987), we obtain an abundance of $(7\pm0.7)\times10^{-11}$ for CH_3C_6H, and of $(9.5\pm0.9)\times10^{-12}$ for CH_3C_5N.

The relative abundance of the isomers CH_2CCHC_4H and CH_3C_6H is, hence, 3.1$\pm$0.3. For the pair of isomers CH_2CCHC_3N and CH_3C_5N, their abundance ratio is 1.3$\pm$0.2.
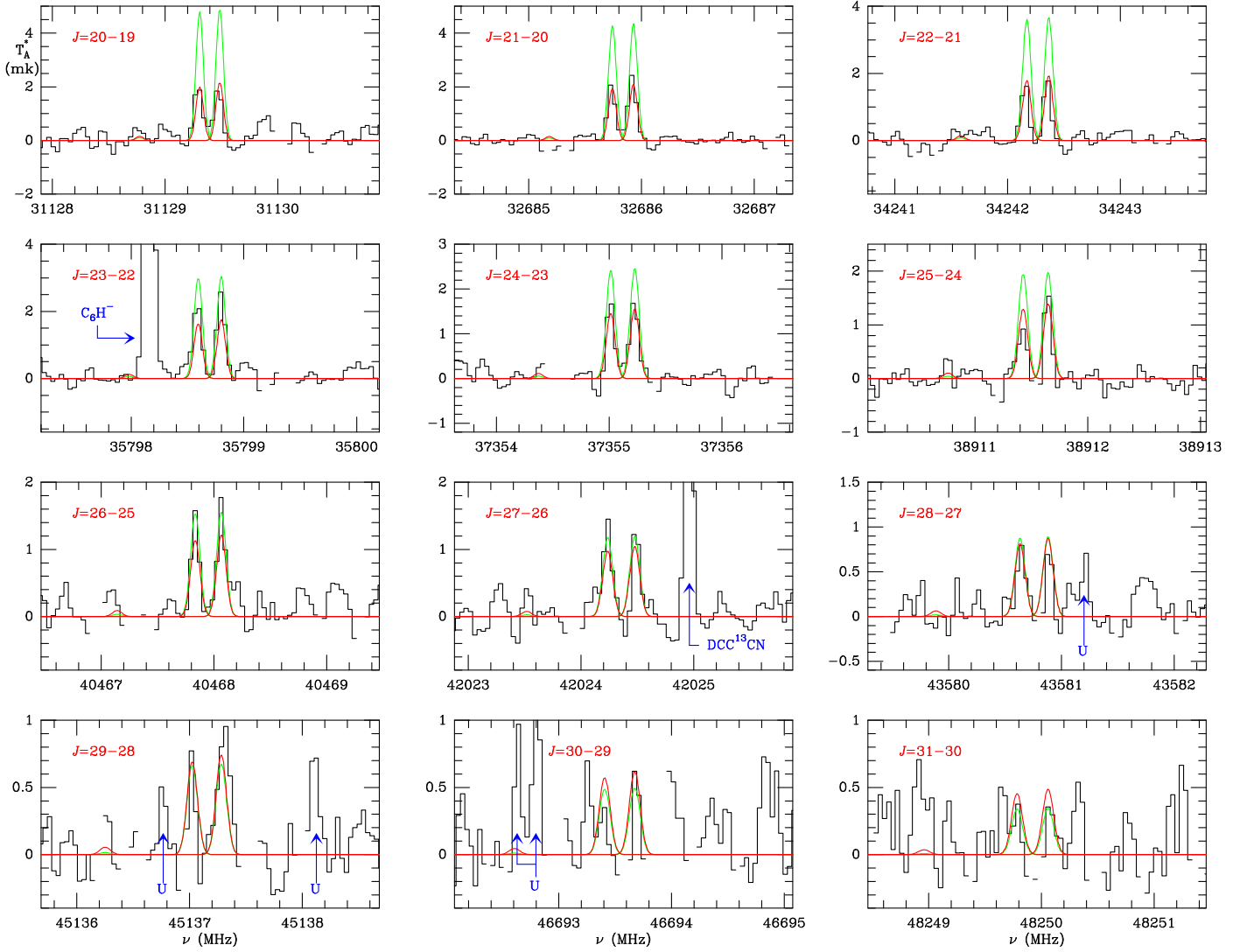
Fig. C.1. Observed transitions of CH_3C_6H in TMC-1. The right component corresponds to K = 0 transitions and the left component to K = 1 transitions. The abscissa corresponds to local standard of rest frequencies. Central frequencies and intensities for the observed lines are given in Table A.1. The ordinate is the antenna temperature, corrected for atmospheric and telescope losses, in milli Kelvin. The quantum numbers of each transition are indicated in the corresponding panel. The red lines show the computed synthetic spectrum for this species for T_{rot} = 9 K and a column density of 7×10^{11} cm^{-2}. The green line shows the computed synthetic spectrum assuming T_{rot} = 6 K and a $N=3.1 \times 10^{12}$ cm^{-2} (Remijan et al. 2006). Blanked channels correspond to negative features produced when folding the frequency-switched data.
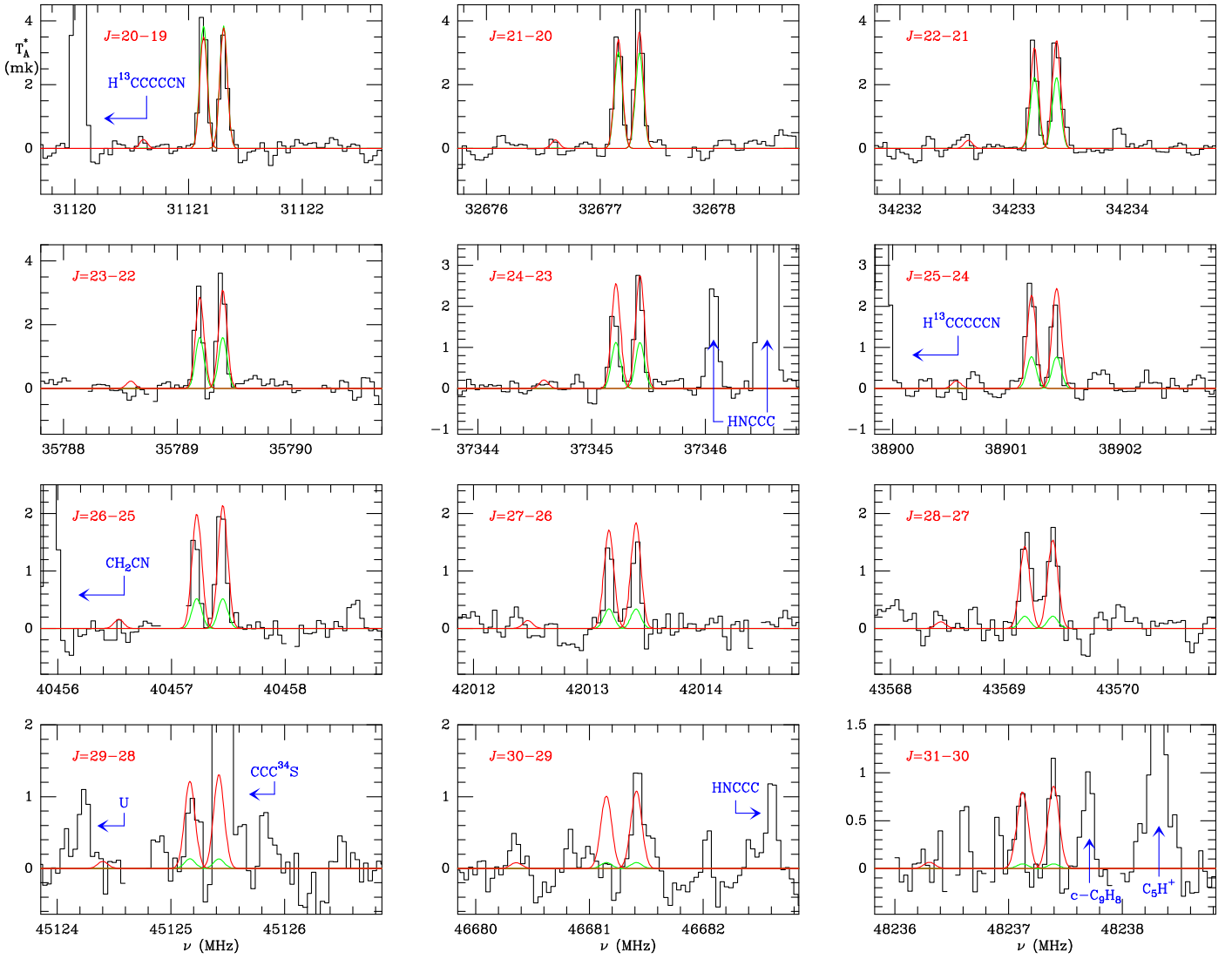
Fig. C.2. Observed transitions of CH$_3$C$_5$N in TMC-1. The right component corresponds to K = 0 transitions and the left component to K = 1 transitions. The abscissa corresponds to the rest frequency of the lines. Frequencies and intensities for the observed lines are given in Table A.1. The ordinate is the antenna temperature, corrected for atmospheric and telescope losses, in milli Kelvin. The quantum numbers of each transition are indicated in the corresponding panel. The red line shows the computed synthetic spectrum for this species for T_{rot} = 9 K and a column density of 9.5×10^{10} cm^{-2}. The green lines show the computed synthetic spectrum adopting T_{rot} = 4 K and N=7.4×10^{11} cm^{-2} (Snyder et al. 2006). Blanked channels correspond to negative features produced when folding the frequency-switched data.